

# Modeling of nano-photonics

Elefterios Lidorikis<sup>a</sup>, Michelle L. Povinelli<sup>a</sup>, Steven G. Johnson<sup>a</sup>, Marin Soljacic<sup>a</sup>,  
Mihai Ibanescu<sup>a</sup>, Yoel Fink<sup>b</sup>, and John D. Joannopoulos<sup>a</sup>

<sup>a</sup>Department of Physics, Massachusetts Institute of Technology, Cambridge, MA 02139

<sup>b</sup>Dept. of Materials Science and Engineering, Massachusetts Institute of Technology  
Cambridge, MA 02139

<http://ab-initio.mit.edu/photons/index.html>

## ABSTRACT

The ability of photonic crystals to mold the flow of light in new ways can lead to a variety of novel and improved designs of optical nanocomponents and nanodevices in photonics. Two examples will be presented: a) Using linear materials, a polarization independent waveguide is designed in a 3D photonic crystal. It is demonstrated that this system provides lossless guiding of light at length-scales approaching the wavelength of the light itself, offering a promising platform for the design of integrated high performance polarization-insensitive waveguide networks. b) Using nonlinear materials, a cylindrical photonic crystal fiber is designed that can exhibit all-optical switching without the need for an axial periodicity. It is shown that this property stems from the unique structure of the cylindrical photonic crystal guided-mode dispersion relation, and can lead to significant improvements in manufacturing ease, operating power usage, and device size requirements, making such a system ideal for integrated all-optical signal processing.

## 1. INTRODUCTION

The amount of digital data transported around the globe grows rapidly every year. Whenever large amount of data has to be transferred, or whenever the data needs to be transferred across large distances, optical fibers are the preferred medium for transportation, due to their low losses, and high capacity. A single optical fiber (whose core is less than 10µm in diameter) has been demonstrated to transmit more than 1Tbit/sec, with losses less than 0.2dB/km. By the same token, this large amount of data needs to be processed. To perform almost any kind of operation on optical signals today (like wavelength conversion, pulse regeneration, bit-rate conversion, logic operation, etc.) the signals first need to be converted to the electronic domain. Unfortunately, there are fundamental physical reasons that prevent electronics from operating well at high frequencies. As a result, the price of electronic components grows rapidly when higher bit-rates are needed, and thus, using all-optical signal processing becomes rapidly more and more appealing.

Since the signal processing needs to be done on ultra-fast scales, the only mechanism at disposal is to exploit a material's optical non-linearities. Most of the research in the area of all-optical devices today is in high-index-contrast integrated optics. Unfortunately, such devices suffer from large losses due to roughness at the surfaces of their waveguides, and are highly polarization sensitive. Another approach involves the use of in-fiber all-optical devices, which would avoid these problems. However, silica fiber non-linearities are very low, which, combined with their large modal area, results into signals having to be propagated for very long distances before the non-linear effects become noticeable. Many interesting switching schemes involving excitation of gap solitons can lower the power requirements, but need a periodic grating along the axial direction, which increases the implementation requirements. In this work we show how the use of photonic crystals can provide a solution for many of these problems.

Photonic crystals<sup>1,2</sup> are periodic dielectric structures that provide a unique control over the flow of light within them. The periodicity is of the order of the wavelength of the light itself. Of central importance is the existence of a photonic band gap, a frequency range for which light propagation is inhibited in all directions. In that sense, the photonic crystal's control over the flow of light can be viewed as the photonic equivalent to the semiconductor's control over the flow of electrons. Impurity levels that trap light at frequencies within the band gap can be designed inside the photonic crystal in terms of suitable structural defects, leading to extremely high Q cavity modes. Similarly, linear arrays of

defects inside a photonic crystal may create guided modes within the band gap, leading to waveguides without any radiation losses.

First, we address the problem of radiation losses and polarization-sensitivity of integrated optical systems. Starting with a 3D photonic crystal integrated platform, we can design waveguides by introducing linear defects into the photonic crystal, such that a guided defect-mode appears within the photonic band gap. It is well known that in such waveguides radiation losses can be completely suppressed, even at features such as sharp bends, while achieving resonant 100% transmission for a wide range of frequencies. It is also well known, however, that photonic crystals, and thus any waveguides created within them, are highly-polarization selective. It may then seem counter-intuitive that such a system could ever be tuned to provide a polarization-insensitive response. We demonstrate that with the correct choice of a 3D photonic crystal, and the utilization of the structure symmetries and the extreme control on the flow of light provided by the photonic crystal, it is possible to do just that. We create doubly-degenerate polarization-insensitive waveguides, that can bend light around sharp corners with high efficiency and zero radiation losses.

Next, we address the problem of in-fiber switching. Recently, a new type of fiber (a photonic band gap fiber called OmniGuide fiber<sup>3</sup>) has been proposed. Materials used in this fiber are chalcogenide glasses which typically have Kerr coefficients 100-1000 times higher than in silica. Furthermore, since this is a high-index contrast fiber, modal areas can be 1000-100 times smaller. Consequently, the non-linear response of these fibers is 4-6 orders of magnitude larger than in silica fibers, making them an ideal non-linear medium. We show that nonlinear gap solitons can exist in such fibers. Gap solitons<sup>4-8</sup> are nonlinear excitations in a medium within which linear (low intensity) propagation is not allowed, and are created by the balance between the strong fiber dispersion and the material nonlinearity. They can be used to implement many all-optical operations<sup>9</sup> including all-optical logic, pulse regeneration and reshaping, creation of ultra-narrow pulses starting from continuous wavelength (CW) signals, etc. Up until now, gap solitons have been exclusively studied in periodically modulated systems, which provide the extremely strong dispersion for frequencies satisfying the Bragg condition, i.e. for frequencies within the band gap. Here we show that because of the unique dispersion relation of the guided modes in photonic band gap fibers, which involves a frequency cut-off at  $k=0$ , we do not need the axial periodicity in order to excite gap solitons. Bistability and optical switching are thus demonstrated for the first time in an axially uniform system. Such systems have small power and implementation requirements, and may be ideal for all-optical in-fiber devices.

We use the finite-difference time-domain (FDTD) method<sup>10</sup> to simulate the propagation of electromagnetic pulses through the photonic crystal structures. We solve the exact full-vector time-dependent Maxwell's equations on a computational grid:

$$\nabla \times \vec{E} = -\mu \frac{\partial \vec{H}}{\partial t}, \quad \nabla \times \vec{H} = \frac{\partial \vec{D}}{\partial t} \quad (1)$$

where the electric displacement  $\vec{D}$  is related to the electric field  $\vec{E}$  by  $\vec{D} = \epsilon \cdot \vec{E}$ . For a Kerr-type nonlinear and isotropic medium, the nonlinear (instantaneous) dielectric constant is  $\epsilon = \epsilon_L + \epsilon_{NL} |\vec{E}|^2$ . For simulating unbounded systems (radiation boundary conditions) we use perfectly-matched-layer (PML) boundary conditions<sup>11</sup> at the edges of the simulation cells.

## 2. POLARIZATION-INDEPENDENT WAVEGUIDES

Lossless guiding of light at length-scales approaching the wavelength of the light itself is a necessary property for any future integrated optical circuit. While high index-contrast dielectric waveguides can reduce radiation losses from features such as sharp bends<sup>12,13</sup>, they cannot completely suppress them and are in general very sensitive to roughness. Photonic crystals<sup>1,2</sup>, on the other hand, have been shown in certain cases to eliminate radiation loss<sup>14,15</sup> and thus offer a promising platform for designing high-performance waveguide networks. A common drawback, however, to all high-index and photonic-crystal waveguide systems proposed to-date (2D<sup>16-19</sup> or 3D<sup>20,21</sup> systems), remains that they are highly polarization selective. Given that the polarization-state of an input signal may not be known and/or may vary over time, their proper operation would require the use of active polarization pre-processing devices. In this work, we demonstrate that by utilizing the symmetries of a proper choice of 3D photonic crystal<sup>22</sup>, one can tune line defects to create guided modes inside the spectral gap that are essentially degenerate, with a polarization-insensitive dispersion relation. We further demonstrate the stability of these modes to symmetry breaking by simulating high-transmission polarization-

independent light guiding around a sharp bend. This is the first structure exhibiting such polarization-insensitive transmission at such length scales.

One approach to polarization insensitivity would be to design a photonic crystal with line defects possessing the appropriate cross-sectional symmetry for polarization degeneracy. Another approach is to employ a photonic crystal consisting of two kinds of photonic crystal slabs, each best suited for confining one of two possible polarizations. The latter approach results in planar arrays of defects, which are amenable to micro-fabrication, and is the method used here. The photonic crystal of Ref. 13 provides precisely this capability, consisting of alternating slabs of dielectric rods in air (*rod* layers, appropriate for confining TM-polarized waves) and air holes in dielectric (*hole* layers, appropriate for confining TE-polarized waves). Wave-guiding structures can be designed within this crystal by introducing planar line defects in the *hole* and/or *rod* layers, resulting in the formation of defect (guided) bands inside the band gap<sup>23</sup>. A remarkable property of this 3D crystal is that the resulting guided modes are very similar to the 2D TE- and TM-polarized modes one gets from solving a 2D problem with the dielectric constant defined by the corresponding cross section along the defect plane<sup>23</sup>. Hence, in the 3D crystal, a sequence of larger holes in a *hole* layer results in a TE-like mode pulled up from the dielectric band, predominantly polarized with its magnetic field normal to the defect plane. Similarly, a sequence of smaller rods in a *rod* layer also results in a TM-like mode pulled up from the dielectric band, but now predominantly polarized with its electric field normal to the defect plane. Note that these modes are approximately even (TE) and odd (TM) under reflection on a plane parallel to the *hole* and *rod* layers. In a purely 2D system this symmetry is exact, prohibiting mode mixing even at lattice distortions such as bends or disorder. This is a key criterion needed to induce a significant suppression of mode mixing at similar planar lattice distortions.

Due to the omnidirectional gap provided by the photonic crystal, the above procedure enables the design of wavelength-scale minimal-loss waveguide networks for both polarizations. While this is promising for integrated optical systems, still, it does not overcome one of integrated optics' old problems: each polarization satisfies a different dispersion relation, resulting in different propagation properties such as speed and pulse broadening, thus leading to a different response in any device. However, if we combine the two sequences of line defects in a way so that the two guided modes are close spatially yet maintain different symmetry, we may tailor the defect structures to enforce an "accidental degeneracy" in the guided dispersion relations, i.e. to have them coincide. In this regard, it is important to identify a symmetry operation along the guide direction, with respect to which the two modes (eigenstates) transform oppositely, so that a tailored defect structure respecting this symmetry will not result in mode mixing and repulsion.

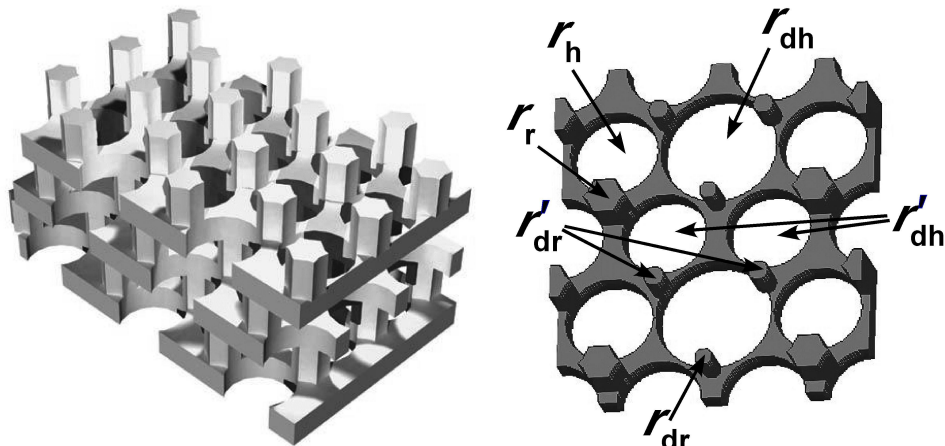


Figure 1. The photonic crystal used in our simulations (left). A schematic of a small segment of the waveguide (right). Only the two layers of the 3D crystal involving the planar line defects are shown for clarity.

A portion of our structure consisting of two layers is shown in Fig. 1. We create our waveguides along the set of  $\{[\bar{2}11]\}$  (second nearest neighbor) directions, because there is a mirror plane perpendicular to the layers, lying along the axis of a straight  $\{[\bar{2}11]\}$  waveguide, for both the *hole*- and *rod*-layer line defects. This distinguishes the TE-like and TM-like modes into different irreducible representations. In contrast, had we chosen a waveguide along the  $\{[0\bar{1}1]\}$

(nearest neighbor) directions, the only symmetry operation that leaves both the *hole*- and *rod*-layer line defects invariant is a 180° rotation along {[0̄1̄1]}. However, this operation cannot distinguish between TE-like and TM-like modes.

The detailed structure of the photonic crystal is reported in Refs. 22 and 23. The hole radius within the *hole* layer is  $r_h=0.414a$  and the equivalent-rod<sup>23</sup> radius within the *rod* layer is  $r_r=0.175a$ , where  $a$  is the in-plane lattice constant and is related to the fcc lattice constant  $a_{\text{fcc}}$  by  $a = a_{\text{fcc}}/\sqrt{2}$ . We use a dielectric contrast of 12, for which a band gap of 21% is obtained. The first step is to introduce two line-defects to create two guided modes of opposite polarization: larger holes ( $r_{dh}=0.53a$ ) in the *hole* layer (which will support the TE-like odd mode) and smaller rods ( $r_{dr}=0.08a$ ) in the *rod* layer (which will support the TM-like even mode). The dispersion relations of these two modes, calculated by the FDTD method, are shown in Fig. 2a. They differ in both their center frequency and their bandwidth. A key property, however, is that they are both well described by a cosine dispersion relation, which makes them easier to match. This cosine dispersion relation arises because our waveguides are very similar to a chain of weakly coupled defects. For stronger coupling, it is expected that the dispersion relations will divert from the simple cosine form and it will thus become progressively difficult to match them. We will use these two bands as a starting point and perturb the surrounding crystal elements (i.e. other holes and rods in the vicinity) to force accidental degeneracy.

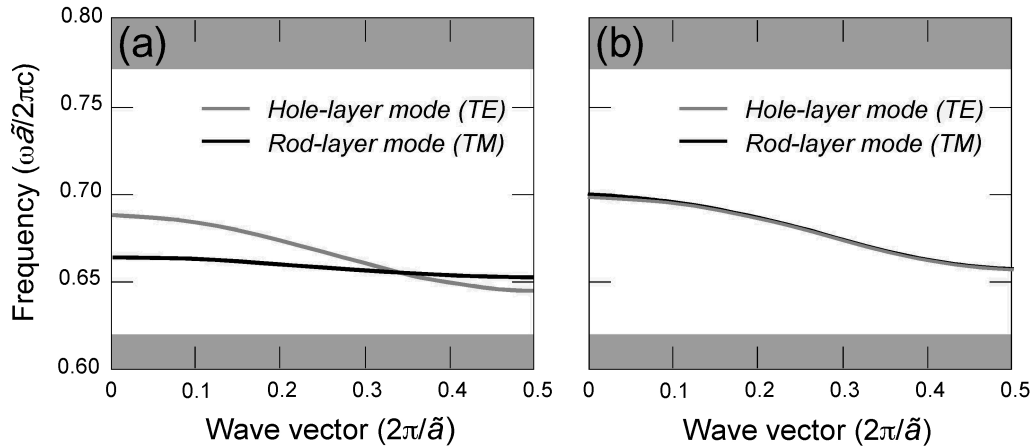


Figure 2. Dispersion relations for the guided modes resulting from planar line defects in the 3D photonic crystal, (a) before and (b) after the tuning. Gray areas mark transmission bands while white areas mark band gaps.

Changes in the dielectric elements around the waveguide can be effectively though as the addition or removal of dielectric material from the high field-intensity regions. These changes will introduce a frequency shift in the corresponding dispersion relations. This shift is maximal for changes in regions of high field intensity, and minimal for changes in regions of low field intensity. Also, the frequency shift is positive when remove dielectric material and negative when we add dielectric material. By looking at the field patterns shown in Fig. 3 for the two modes at two different propagation constants, we immediately make the following two observations. Changing the elements that “make up” the waveguide (i.e. the holes with radius  $r_{dh}$  and rods with radius  $r_{dr}$ ) will have a similar effect for both wave vectors, resulting in to an almost uniform shift of the dispersion curve. On the other hand, changing the neighboring elements to the waveguide (i.e. the holes with radius  $r'_{dh}$  and rods with radius  $r'_{dr}$ ), will have a minimal effect for  $k=0.5$ , but a significant effect for  $k=0$ , resulting in to a non-uniform shift of the dispersion curve. This later change is thus useful for changing the bandwidth of a mode. It is apparent that combining suitable changes for all these elements will enable us to enforce accidental degeneracy between the two modes.

For simplicity, we limit ourselves to changes in radius only. We adopt an empirical approach where we fit the effect of different radius perturbations, and combine them through a conjugate-gradient search algorithm to find the combination producing the desired degeneracy. By combining two perturbations per layer we find a range of defect parameters that result in degenerate bands, each at a different center frequency and bandwidth. A parameter set requiring small radius changes is  $r_{dh}=0.55a$ ,  $r'_{dh}=0.40a$ ,  $r_{dr}=0.085a$ , and  $r'_{dr}=0.10a$  for the two hole and rod radii, respectively (see Fig. 1). The corresponding dispersion relations demonstrating the degeneracy are shown in Fig. 2b (additional bands are slightly pulled-up from the “dielectric” band as well, but are not shown here since they do not come close to our modes of interest). The resulting “doubly-degenerate” guided mode has a bandwidth of about 6% of its center-frequency and a

group velocity at the Brillouin-zone center of about  $0.13c$ . This is the first 3D photonic crystal structure for which a polarization-independent dispersion relation has been demonstrated.

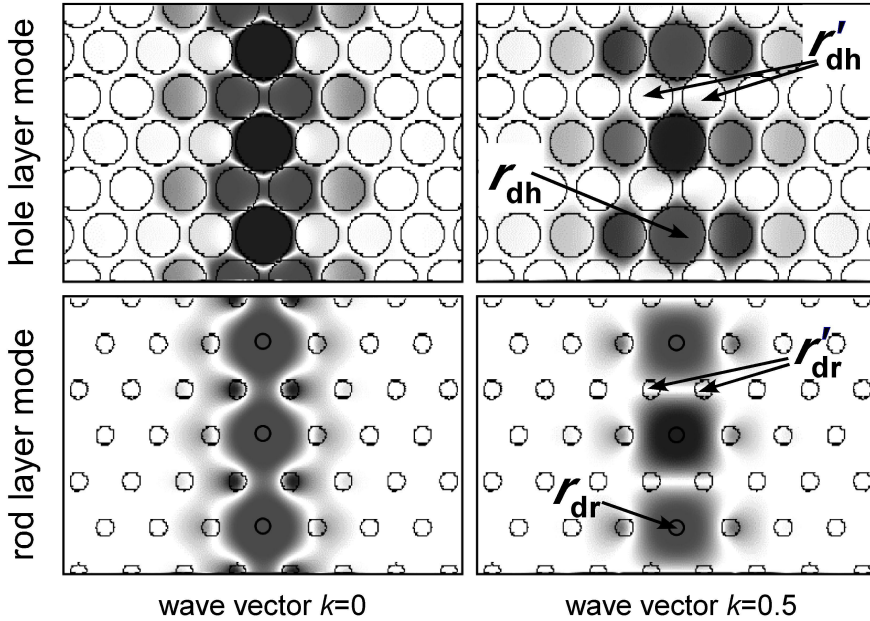


Figure 3. The fundamental two waveguide modes. The TE-like mode of the *hole* layer (top panels), and the TM-like mode of the *rod* layer (bottom panels). These are plotted at a wave vector  $k=0$  (left panels) and  $k=0.5(2\pi/\tilde{a})$  (right panels).

A natural and important question is to what degree this degeneracy maintains a polarization-independent response in cases where we break symmetry, such as at a sharp bend. To answer this, we study a system that involves a  $60^\circ$  bend, as depicted in the top panel of Fig. 4. Unfortunately, the two layers are not equivalent at the bend. While in the *hole*-layer structure we have a smooth transition between the two straight waveguide-branches, in the *rod*-layer the bend creates a nearest neighbor coupling of two rods of radius  $r_{dr}$  (normally second-nearest-neighbor coupling in the straight waveguide). In fact, there is no way to make both layers have a smooth transition between their two branches. As we shall see, this introduces slightly different high-transmission resonance conditions for each polarization. In addition, there will be some mixing between the two polarization states at the bend, where the mirror symmetry is destroyed.

We use the FDTD method to simulate the propagation of electromagnetic pulses through the bend. The computational system is taken very large to assure clear separation among the various pulses. It consists of a cell of size  $72\tilde{a} \times 16a \times 2a_v$ , where  $\tilde{a}$  is the lattice period along the propagation direction,  $\tilde{a} = \sqrt{3}a = \sqrt{3}/2a_{fcc}$ , and  $a_v$  is the lattice period along the vertical [111] direction (3 bilayers),  $a_v = \sqrt{6}a = \sqrt{3}a_{fcc}$ . The bend is located at a distance of  $48\tilde{a}$  from the entrance of the input waveguide. We use PML boundary conditions in the propagation direction, and periodic boundary conditions in the other two directions. The waveguide region after the bend is “wrapped around” using the periodic boundary conditions, minimizing the required size of the computational cell.

A pulse with a Gaussian profile in time is launched at the entrance of the waveguide, and the fields are monitored at two positions, as shown in Fig. 4. Position A is located halfway between the source and the bend and is the observation point for the incident and reflected pulses, while position B is located  $12\tilde{a}$  after the bend and is the observation point for the transmitted pulse. Minimal secondary reflections at the edges of the computational cell are still present, but they appear at later times and do not contaminate the useful data. We find that most of the energy is transmitted through the bend. As expected, the symmetry breaking at the bend results in transmitted and reflected pulses that are composed of both modes. However, this mixing is very small, comparable to half the overall reflection from the bend (see Fig. 4).

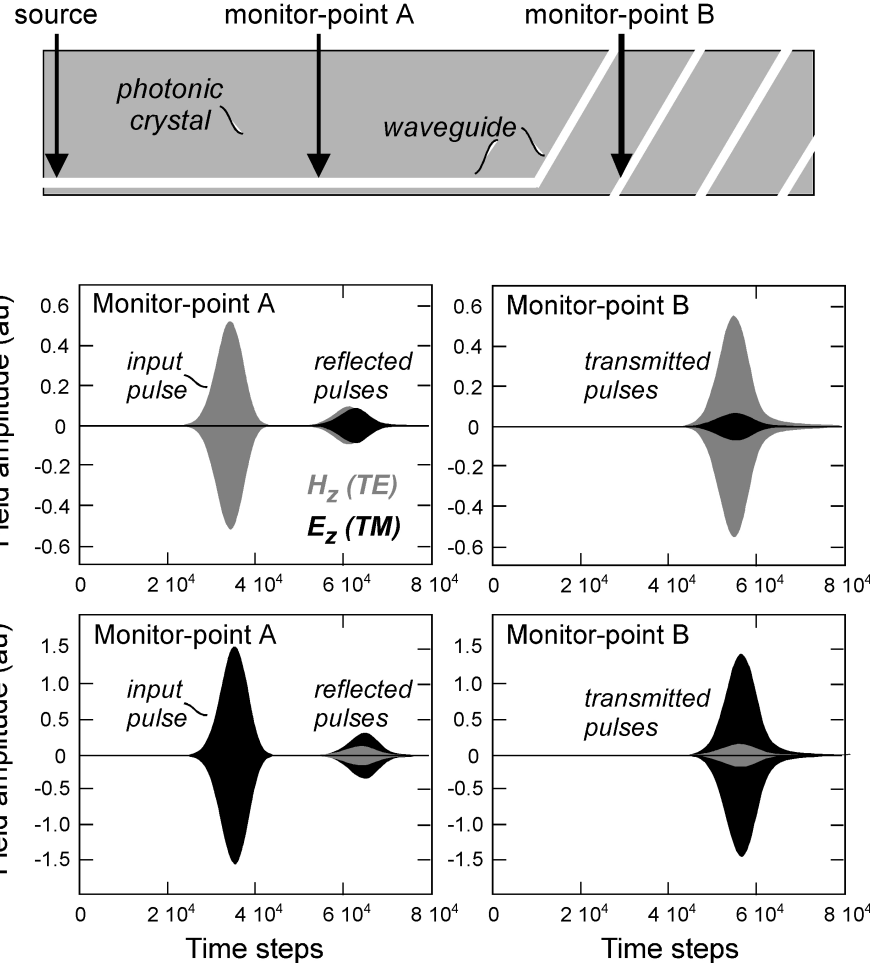


Figure 4. Top panel: Schematic of the simulation system for studying transmission through a bend. The waveguide, defined by the white line, “wraps around” after the bend using periodic boundary conditions, minimizing the required computational cell. Monitor points are at A and B. Bottom panels: Simulation results. Fields at the observation points A and B, which are located before and after the bend respectively. Each polarization is studied separately with points A and B centered in the appropriate layer in each case. Gray is used for the  $H_z$  field of the TE-like mode and black for the  $E_z$  field of the TM-like mode. A pure TE(TM)-like mode will have zero  $E_z$  ( $H_z$ ) field at its symmetric center, as is the case for the incident pulses.

In order to quantify the transmission through the bend, we study the frequency-resolved pulses going in and out of the bend. Since these are not single-mode waveguides, we must use data from flux-monitoring planes, positioned at A and B. For better resolution, as well as a consistency test, we use two pulses of different center frequencies per polarization, as shown in the top panels of Fig. 5. The corresponding ratios of the fluxes at A and B provide the transmission and reflection coefficients, as shown in the bottom panel of Fig. 5. These coefficients add up to 1 for all frequencies, with an error of less than 1%. We find a wide frequency range of high transmission for both modes, and a frequency  $\omega\tilde{a}/2\pi c=0.6835$  for which the transmissions coincide to 94.5%. Note that, as expected, resonant transmission is observed at different frequencies for the two modes: at lower frequencies for the TE-like mode and higher frequencies for the TM-like mode. Also note that the TM mode does not actually achieve 100% transmission at any frequency within the useful bandwidth. Further tuning of the bend region could lead to 100% transmission of this mode if desired.

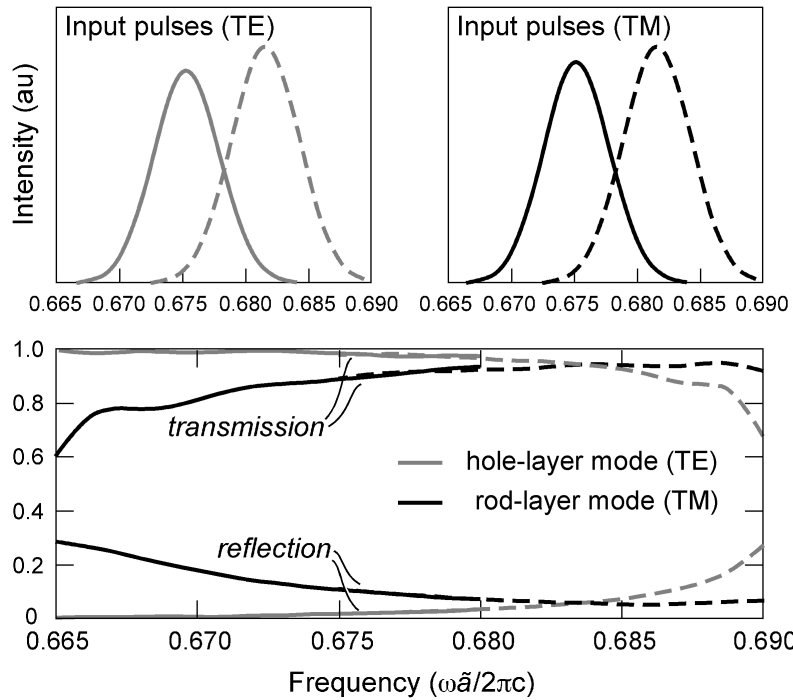


Figure 5. Top panels: Spectral profile of the input pulses used in the numerical experiments for the TE-like and the TM-like modes. Bottom panel: By taking appropriate ratios of transmitted, reflected and input pulses we extract the corresponding transmission and reflection coefficients.

Around the common transmission frequency, we resolve the calculated fluxes into the two modes, in order to quantify the degree of modal mixing. We find that mixing is generally small, and that it monotonously decreases for increasing frequency (from about 5% at  $\omega\tilde{a}/2\pi c=0.675$  to less than 1% at  $\omega\tilde{a}/2\pi c=0.69$ ). At the common high-transmission frequency, the transmitted power retains its polarization to about 97%. The absence of strong modal mixing is due to the approximate horizontal mirror plane symmetry, as was mentioned earlier. The TE-like and TM-like modes appear as two different representations of a single horizontal symmetry plane, thus resulting in minimal mode mixing in the bend region. An important point to note here is that the field pattern of the two modes is different. This will manifest into different coupling coefficients with a symmetric input such as from a fiber. It will thus be necessary to tailor the input part of the waveguides in order to match the coupling coefficients, and thus achieve polarization-insensitive excitation. This however, goes beyond the scope of this paper.

We have demonstrated high (~95%) transmission through a sharp bend, with a high degree (~97%) of polarization insensitivity, for certain frequencies. Two improvements can be achieved by optimizing the crystal structure at the bend: i) an increase of the symmetry at the bend, so that less mode mixing occurs, and ii) a change of the resonant-transmission conditions for the two modes so that they better coincide. Thus, there are enough degrees of freedom for optimization that ultimately, it should be possible to achieve 100% polarization-independent transmission through sharp bends in this system.

In addition to guiding light around sharp corners, such fine-tuned waveguide structures are ideal for miniaturized passive polarization-processing components. Because each polarization is primarily guided in a different layer, it is very easy to separate the two modes. We can easily imagine designing devices such as polarization splitters (each mode bends into a different branch of a junction), or polarization rotators (one mode tunneling to the other by resonant mode mixing). These structures may thus prove to be very useful in future integrated all-optical systems. In contrast, had we employed the alternative approach of designing a photonic crystal with line defects possessing the appropriate cross-sectional symmetry for polarization degeneracy, such operations would be more difficult, as both modes would be primarily guided by the same crystal elements.

## 2. GAP SOLITONS IN AXIALLY UNIFORM FIBERS

Gap solitons and optical switching<sup>4-8</sup> have been extensively studied in nonlinear dielectric structures with a one-dimensional axial periodicity in their linear refractive properties. Corresponding experimental realizations include waveguide<sup>24</sup> or fiber Bragg gratings<sup>25,26</sup> and integrated multi-layer heterostructures<sup>27,28</sup>. Such periodic systems exhibit spectral gaps of high reflectivity for wave-propagation along the axial direction. For intense light illumination at a frequency inside one of the gaps and with an optical nonlinearity present, these systems can exhibit solutions whose envelopes take the form of solitary waves. Such solutions, called gap-solitons or Bragg-solitons, introduce a strong power-dependence to the transmissivity, at some powers achieving even full resonant transmission. In some cases a bistable response may be observed, i.e. one of two different transmissivities are possible at the same input power, making the actual optical response a function of the system's history. Such periodic structures are very attractive for all-optical switching, logic-gate operation, memory etc<sup>9</sup>.

Because of the necessity of a spectral gap for their existence, gap solitons and gap-soliton-mediated bistability have been exclusively studied in systems with axial periodicity. In this work, we show that gap-soliton excitation is also possible in axially-uniform photonic bandgap (PBG) fibers<sup>3,29</sup>. These fibers are laterally grated forming a PBG cladding that surrounds the core. Guiding is achieved through a cladding gap-condition, in contrast to usual fibers where guiding is achieved through total internal reflection. We show that in the presence of an optical Kerr-type nonlinearity, such axially-uniform PBG fibers exhibit gap-soliton generation and gap-soliton-mediated bistability. The observed nonlinear response is a direct consequence of the particular guided-mode dispersion relation, which involves a frequency cut-off at  $k=0$ , and is unique among axially uniform systems to high index-contrast PBG fibers, and metallic waveguides.

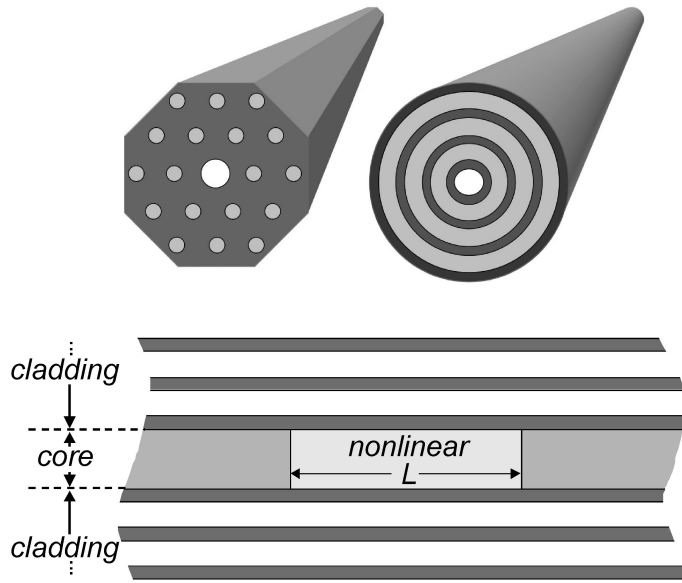


Figure 6. Top: Schematics of two photonic band gap fibers, the Holey fiber and the Omnidirectional fiber respectively. Bottom: The 2D simulation system which is an embodiment of the Omnidirectional fiber: cladding consists of alternating dielectric layers of high-index (2.8) with thickness  $0.3a$  and low-index (1.5) with thickness  $0.7a$ , where  $a$  is the period of the cladding layers and serves as the unit of length. The core has a diameter  $d_{\text{linear}}=d_{\text{nonlinear}}=1.2a$  and consists of linear material (darker gray) with index  $n=1.9$  and nonlinear material (lighter gray) with index  $n'=n_0+n_2|E|^2$ , where  $n_0=1.6$ . The guiding direction is parallel to the layers.

We study a two-dimensional embodiment of PBG fibers<sup>30</sup>, described fully in Fig. 6. This system captures the most essential features of the 3D fiber, in particular, guided-mode dispersion relations with a frequency cut-off at  $k=0$ , and the absence of a full spectral gap. For example in Fig. 7a we superimpose the dispersion relations for the linear material and for the nonlinear material when  $n'=n_0=1.6$ , as calculated by the FDTD method. In each case there is a frequency cut-off

at  $k=0$  which we denote as  $\omega_c$  for the linear material and  $\omega'_c$  for the nonlinear material. The difference in refractive index results in an almost parallel shift in dispersion relations. Any other choice of refractive indexes and structural parameters should suffice as long as one has single mode operation and  $\omega'_c > \omega_c$ . For example, setting  $n=n_0 \geq 1$  and shrinking the nonlinear core  $d_{\text{nonlinear}} < d_{\text{linear}}$  would have a similar effect, since guided modes with a reduced modal area appear at a higher frequency, and thus with an increased cut-off frequency. This is particularly important in terms of implementation and applications, since there exist many easy ways for externally controlling the dispersion relation, such as mechanical strain, temperature, radiation, etc.

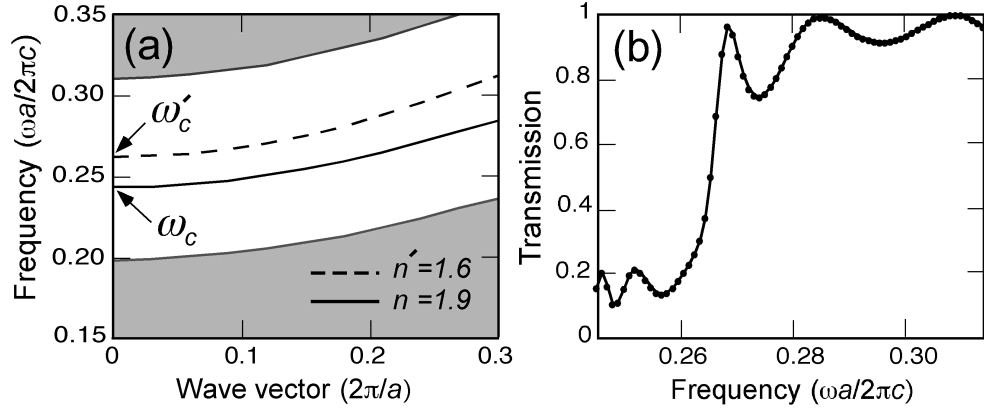


Figure 7. (a) Dispersion relations calculated by the FDTD method for two values of the core index. The cut-off frequencies are  $\omega_c = 0.244$  and  $\omega'_c = 0.26215$ . Gray areas represent cladding and radiation modes, where light is either guided through the cladding or escapes out of the fiber. These modes cover the entire frequency region at higher wave vectors. (b) Transmission coefficient vs frequency for a linear-material system with an  $n'=n_0=1.6$  defect core of size  $L=5a$ .

At low input power, guided waves in the linear-material core (i.e.  $\omega > \omega_c$ ) should be strongly reflected upon incidence on the nonlinear region if  $\omega < \omega'_c$ . Such a linear transmission coefficient is shown in Fig. 7b. At high input power, however, we should observe a wide range of nonlinear phenomena, similar to those found in the study of nonlinear periodic gratings. For example, a power-dependent frequency shift of the nonlinear-material's dispersion relation should result into a power-dependent transmission, such as in optical limiting systems. For the proper sign of  $n_2$  ( $n_2 > 0$  in our case), we should also observe the excitation of resonant structures such as gap solitons, resulting in resonant transmission and bistability. It is the latter effects in the limit of small nonlinearities (which is the experimentally correct limit anyway) that will be our focus here.

To explore these effects in detail, we perform time-domain simulations for the system shown in Fig. 6 using the FDTD method, which, apart from the discretization error, gives exact solutions to the full-nonlinear time-dependent Maxwell's equations. In figure 8 we plot the fiber's nonlinear response for two nonlinear-core lengths,  $L = 5a$  and  $L = 8a$ . A CW excitation with a frequency tuned below the cut-off  $\omega'_c$  is the input for both cases. The electromagnetic fields and flux are monitored at the output beyond the nonlinear core, while PML boundary conditions are used to simulate perfect absorption at the edges of the computational cell.

We obtain two types of response: i) CW: observed in the smaller  $L = 5a$  system, involving bistable switching between a CW low- and a CW high-transmission state (Figs. 8a and 8b). ii) Pulsating: observed in the larger  $L = 8a$  system, involving bistable switching between a stable low- and a pulsating high-transmission state (Figs. 8c and 8d). Such dual response is well known in grating systems. The steady state is the result of the excitation of a stationary gap-soliton in the structure. In Fig. 10 we plot the field intensity profile along the nonlinear core for the resonant transmission point, which clearly shows the excitation of a gap soliton. Incident waves coupling with it achieve high resonant-transmission even though they are tuned to a gap frequency. The transition from a steady solution to a pulsating one is related to an instability that occurs when the ratio of the gap-soliton's width to the nonlinear core's length becomes small<sup>8</sup>. When this is the case, the excited gap-soliton propagates along the core, resulting in a series of propagating solitons, or, a soliton train, and thus an output that consists of a periodic series of pulses. This alternative method of energy transfer, nevertheless, also results in high transmission.

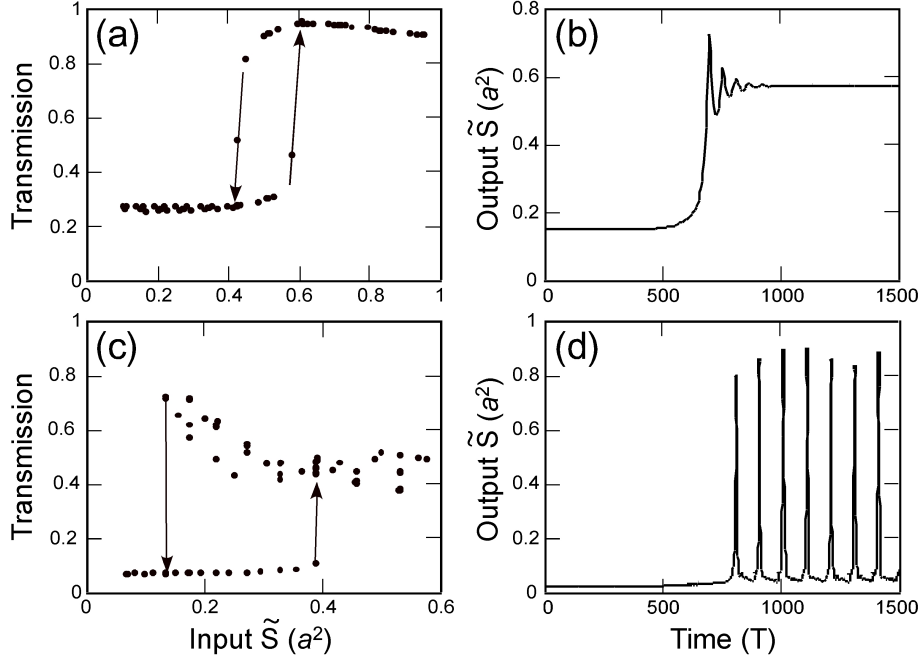


Figure 8. (a) Transmission vs input flux  $\tilde{S}$  for the  $L=5a$  system and  $\omega a/2\pi c=0.26$ . The normalized flux  $\tilde{S}$  is defined as  $\tilde{S}=n_0 \cdot n_2 \cdot S$ , where  $S$  is the electromagnetic flux through the fiber's cross section. (b) Output flux during switch-up (path marked by the up-pointing arrow) for the  $L=5a$  system. (c) and (d) Same as (a) and (b), but for the  $L=8a$  system. The unit of time in (b) and (d) is the incident-wave period  $T=2\pi/\omega$ .

In Fig. 9 we plot the intensity along the nonlinear core as a function of time, around the switch-up point for the  $L=5a$  system (CW response). It can be seen how the gap soliton is excited in the structure. At first it undergoes a damped oscillation until it reaches equilibrium. These oscillations are well correlated with the fluctuations of the output in Fig. 8b. This transient time is a measure of the response (switching) time of our device, which is of the order of 200 periods (for  $\lambda=1.55\text{mm}$  this time is about 1ps). A similar plot (not shown), but inverted and with less fluctuations is obtained at the switch-down point. In the  $L=8a$  case, on the other hand, these oscillations are not damped, and so the soliton does not reach equilibrium, but rather it gets transmitted out of the nonlinear core, only to be followed by a new soliton, resulting into a periodic train of pulses in the output. The peak intensity of each pulse is about 10 times larger than that of an equivalent transmitted CW. The duration of each pulse is about 20 periods and the pulses appear at a frequency of about 100 periods (for  $\lambda=1.55\text{\mu m}$  this is a pulse width of about 100 fs at a period of about 500 fs). In Fig. 10 we plot the intensity along the nonlinear core for the  $L=5a$  system at two different points: at the peak of the upper transmission branch where a gap soliton has been excited (at time $\approx 900T$  of Fig. 9), and at the lower branch where the wave decays exponentially (at time $\approx 400T$  of Fig. 9).

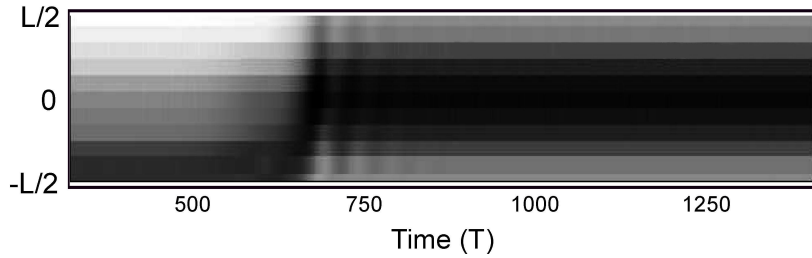


Figure 9. Intensity along the nonlinear core as a function of time, around the switch-up point for the  $L=5a$  system (CW response). Darker regions mark higher intensity. The vertical axis is the axial (propagation) direction, with the input is at  $-L/2$  and the output at  $L/2$ . Before the switch-up, the intensity decays along the axial direction, while after switch-up, the intensity is maximum in the center of the nonlinear core, corresponding to a gap soliton.

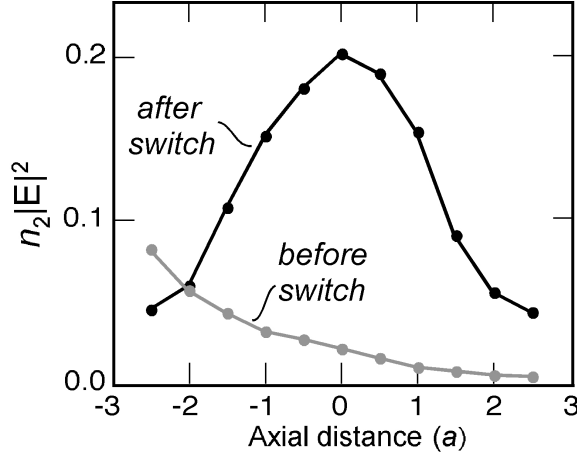


Figure 10. Normalized intensity (or local index change  $\delta n = n_2 |E|^2$ ) along the nonlinear core for the  $L=5a$  system at, the peak (100% resonant transmission) of the upper transmission branch (black), and, at the lower transmission branch (gray). The excitation of a gap soliton is seen at the resonant transmission case.

Our axially uniform nonlinear system responds very similarly to a nonlinear Bragg grating system. However, it is different in terms of performance and implementation. Having no need for a periodic modulation it is easier to make. Materials used in these fibers are chalcogenide glasses which are highly nonlinear, and so all that is needed is a frequency cut-off. This can be achieved by replacing part of the core with a lower index nonlinear material (as we did here), or alternatively, it can be achieved by external means, such as mechanical strain, temperature, radiation, etc. For example, shrinking part of the core by externally creating a constriction will have the same effect in creating a frequency cut-off. Given that the device's mode of operation (CW or pulsed) depends on the device structural parameters, we can use these external means to control its operation, without having to change the input power or frequency.

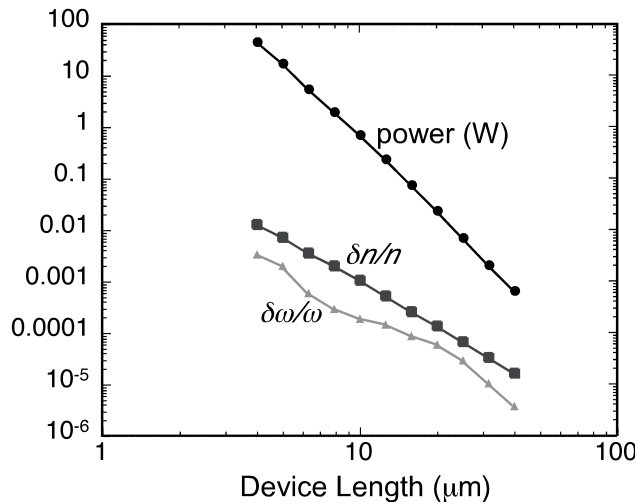


Figure 11. Power and bandwidth requirements for the proposed device as a function of its nonlinear core size, for chosen parameters  $\lambda=1.55 \mu\text{m}$  and  $n_2=1.5 \times 10^{-13} \text{ cm}^2/\text{W}$ . Power is measured at the switch-up point at which the width of the bistable loop is 10% of its mid-input power. Bandwidth  $\delta\omega/\omega$  is the frequency change necessary to change the switch-up power by 10%.

Finally, we used a simplified 1D nonlinear model based on a fit of the dispersion relations of Fig. 7a, to estimate how various experimental parameters would depend on the system's size  $L$ . We do not present details of this model here. We have found the 1D model's predictions to agree well with the simulation data and it is thus a valid and useful tool for practical estimates. We calculated the operating power  $P$ , the maximum nonlinear index change induced  $\delta n/n$  and the operational bandwidth  $\delta\omega/\omega$  as a function of  $L$ , while we tuned the frequency so that the width of the bistable loop is

10% of its center intensity. These results are shown in Fig. 11. We find that all three quantities drop exponentially with increasing size  $L$ . As a quantitative example, a system with an nonlinear core length of  $L=10\mu\text{m}$  operating at a vacuum wavelength of  $\lambda=1.55\mu\text{m}$  (i.e.  $a=0.406\mu\text{m}$ ) and with a nonlinear coefficient of  $n_2 = 1.5 \cdot 10^{-13} \text{ cm}^2/\text{W}$  (typical of many chalcogenide glasses), requires an operating power of about  $P=800\text{mW}$ , a maximum nonlinear-index-change of about  $\delta n/n=0.001$ , and offers a bandwidth of about  $\delta\omega/\omega=0.0002\approx40\text{GHz}$ .

### 3. CONCLUSIONS

In conclusion, we have shown two cases where the use of photonic crystals can lead to novel and improved designs of optical nanocomponents and nanodevices in photonics. a) We have shown that polarization-independent waveguides and waveguide bends can be designed in a particular class of 3D photonic crystals by means of forced accidental degeneracy. The only requirement is the existence of two well-localized modes of definite and opposite symmetry. Further improvements and/or creation of novel polarization-processing devices should be possible by optimizing the structure parameters. b) We have studied an axially uniform nonlinear system that exhibits gap-soliton formation and optical switching. This ability to obtain soliton formation and switching without imposing axial periodicity may lead to new design and fabrication opportunities for eventual experimental realization of all-optical nanodevices.

### 4. ACKNOWLEDGEMENTS

This research was supported in part by, the U.S. Army through the Institute for Soldier Nanotechnologies, under Contract DAAD-19-02-D0002 with the U.S. Army Research Office, and the Materials Research Science and Engineering Center program of the National Science Foundation under Grant No. DMR-9400334. Computations were performed at the Pittsburgh Supercomputing Center.

### REFERENCES

1. J.D. Joannopoulos, R.D. Meade, and J.N. Winn, *Photonic Crystals* (Princeton, New York, 1995).
2. For recent work, see, e.g., *Photonic Crystals and Light Localization*, edited by C.M. Soukoulis, Proceedings of the NATO ASI on Photonic Band Gap Materials, Limin Hersonissou, Crete, Greece, 19-30 June 2000 (Kluwer Academic, Dordrecht, 2001).
3. Y. Fink, D.J. Ripin, S. Fan, C. Chen, J.D. Joannopoulos, and E.L. Thomas, J. Lightwave Tech. 17, 2039 (1999); S.G. Johnson, M. Ibanescu, M. Skorobogatiy, O. Weisberg, T.D. Engeness, M. Soljacic, S.A. Jacobs, J.D. Joannopoulos, and Y. Fink, Optics Express 9, 748 (2001); B. Temelkuran, S.D. Hart, G. Benoit, J.D. Joannopoulos, and Y. Fink, NATURE 420, 650 (2002).
4. H.G. Winful, J.H. Marburger, and E. Garmire, Appl. Phys. Lett. 35, 379 (1979).
5. Wei Chen and D.L. Mills, Phys. Rev. Lett. 58, 160 (1987); Phys. Rev. B 36, 6269 (1987); D.L. Mills and S.E. Trullinger, Phys. Rev. B 36, 947 (1987)
6. J.E. Sipe and H.G. Winful, Opt. Lett. 13, 132 (1988); C. Martijn de Sterke and J.E. Sipe, Phys. Rev. A 38, 5149 (1988).
7. D.N. Christodoulides and R.I. Joseph, Phys. Rev. Lett. 62, 1746 (1989).
8. C. Martijn de Sterke and J.E. Sipe, Phys. Rev. A 42, 2858 (1990).
9. B.E. Saleh and M.C. Teich, *Fundamentals of Photonics* (Wiley, New York, 1991).
10. K.S. Kunz and R.J. Luebbers, *The Finite-Difference Time-Domain Methods* (CRC, Boca Raton, FL, 1993).
11. J.C. Chen, and K. Li, Microwave Opt. Tech. Lett. 10, 319 (1995).
12. M. Majd, B. Schuppert, and K. Petermann, IEEE Photonics Techn. Lett. 5, 806 (1993); M. Heinbach, M. Schienle, A. Schmid, B. Acklin, and G. Muller, J. Lightwave Techn. 15, 833 (1997); J.S. Foresi, D.R. Lim, L.

- Liao, A.M. Agarwal, and L.C. Kimerling, proc. SPIE **3007**, 112 (1997); M. Rajarajan, S.S.A. Obayya, B.M.A. Rahman, K.T.V. Grattan, and H.A. El-Mikati, SBMO/IEEE MTT-S IMOC Proceedings vol. **2**, 462 (1999).
13. C. Manolatou, S.G. Johnson, S. Fan, P.R. Villeneuve, H.A. Haus, and J.D. Joannopoulos, *J. Lightwave Technol.* **17**, 1682 (1999).
  14. A. Mekis, J.C. Chen, I. Kurland, S. Fan, P.R. Villeneuve, and J.D. Joannopoulos, *Phys. Rev. Lett.* **77**, 3787 (1996).
  15. J.D. Joannopoulos, P.R. Villeneuve, and S. Fan, *Nature* **386**, 143 (1997).
  16. M. Tokushima, H. Kosaka, A. Tomita, and H. Yamada, *Appl. Phys. Lett.* **76**, 952 (2000).
  17. E. Chow, S.Y. Lin, J.R. Wendt, S.G. Johnson, and J.D. Joannopoulos, *Opt. Lett.* **26**, 286 (2001).
  18. J. Moosburger, M. Kamp, A. Forchel, S. Olivier, H. Benisty, C. Weisbuch, and U. Oesterle, *Appl. Phys. Lett.* **79**, 3579 (2001).
  19. A. Talneau, L. Le Gouezigou, N. Bouadma, M. Kafesaki, C.M. Soukoulis, and M. Agio, *Appl. Phys. Lett.* **80**, 547 (2002).
  20. B. Temelkuran and E. Ozbay, *Appl. Phys. Lett.* **74**, 486 (1999); M. Bayindir, E. Ozbay, B. Temelkuran, M.M. Sigalas, C.M. Soukoulis, R. Biswas, and K.M. Ho, *Phys. Rev. B* **63**, 081107(R) (2001).
  21. A. Chutinan and S. Noda, *Appl. Phys. Lett.* **75**, 3739 (1999); S. Noda, K. Tomoda, N. Yamamoto, and A. Chutinan, *Science* **289**, 604 (2000).
  22. S.G. Johnson and J.D. Joannopoulos, *Appl. Phys. Lett.* **77**, 3490 (2000).
  23. M.L. Povinelli, S.G. Johnson, S. Fan, and J.D. Joannopoulos, *Phys. Rev. B* **64**, 075313 (2001).
  24. N.D. Sankey, D.F. Prelewitz, and T.G. Brown, *Appl. Phys. Lett.* **60**, 1427 (1992).
  25. B.J. Eggleton, C. Martijn de Sterke, and R.E. Slusher, *J. Opt. Soc. Am. B* **14**, 2980 (1997).
  26. D. Taverner, N.G.R. Broderick, D.J. Richardson, R.I. Laming, and M. Ibsen, *Opt. Lett.* **23**, 259 (1998); *Opt. Lett.* **23**, 328 (1998).
  27. M. Cada, J. He, B. Acklin, M. Proctor, D. Martin, F. Morier-Genoud, M.-A. Dupertuis, and J.M. Glinski, *Appl. Phys. Lett.* **60**, 404 (1992); S. Janz, J. He, Z.R. Wasilewski, and M. Cada, *Appl. Phys. Lett.* **67**, 1051 (1995).
  28. P. Millar, R.M. De La Rue, T.F. Krauss, J.S. Aitchison, N.G.R. Broderick, and D.J. Richardson, *Opt. Lett.* **24**, 685 (1999).
  29. R.F. Gregan, B.J. Mangan, J.C. Knight, T.A. Birks, P.St.J. Russell, P.J. Roberts, and D.C. Allan, *Science* **285**, 1537 (1999).
  30. M. Soljacic, M. Ibanescu, S.G. Johnson, Y. Fink , and J.D. Joannopoulos, *Phys. Rev. E* **66**, 055601R (2002); M. Soljacic, M. Ibanescu, S.G. Johnson, J.D. Joannopoulos, and Y. Fink, *Opt. Lett.* **28**, 516 (2003).